Correlation of the radio continuum, infrared, and CO molecular emissions in NGC 3627 [*]

R. Paladino[1], M. Murgia[1,2], A. Tarchi[1,2], L. Moscadelli[3], and C. Comito[4]

[1] INAF - Osservatorio Astronomico di Cagliari, Loc. Poggio dei Pini, Strada 54, I-09012 Capoterra (CA), Italy
[2] INAF - Istituto di Radioastronomia, Via Gobetti 101, I-40129 Bologna, Italy
[3] INAF - Osservatorio Astrofisico di Arcetri, Largo E. Fermi, n. 5, I-50125, Firenze, Italy
[4] MPI, Bonn. Max-Planck-Institut füer Radioastronomie, Auf dem Hüegel 69, D-53121 Bonn, Germany

ABSTRACT

Aims. We present new radio observations of two regions of the spiral galaxy NGC 3627, including new radio continuum observations at 1.4 GHz with the Very Large Array, and also new observations in the CO line, taken with the Plateau de Bure interferometer. Comparing these observations with archival *Spitzer* and H_α data we study the correlation of the radio continuum (RC), infrared-$8\mu m$, and CO emissions at a spatial resolution of 100 pc.
Methods. We compare the point-by-point variations of the RC, CO, and $8\mu m$ brightnesses in two distinct regions of 2 kpc × 2 kpc in size of NGC 3627. We also present a three-dimensional fit of the observed data.
Results. We examined scale much lower than the electron diffusion scale, where a breakdown of the correlations would be expected. However, no evidence for such correlation breakdown has been found. The RC emission follows the distribution of CO well, and the widths of several structures, measured along slices across them, are comparable. Furthermore, we found that down to a spatial scale of 100 pc, the radio continuum emission is correlated with dust emissions at 4.5, 5.8, and 8 μm, which trace different dust temperatures. We present a new perspective, a three-dimensional representation, with which to visualize and study the RC-CO-$24\mu m$ and RC-CO-$8\mu m$ correlations. We fit the observed data with a three-dimensional line, obtaining a rms of 0.25 dex.
Conclusions. The observed correlation enhances the complexity of the electrons diffusion, losses, and injection mechanisms, and of their connection to star formation processes described by molecular and dust emissions. We plan to further investigate this connection using spatially resolved spectral index studies at low radio frequencies where the thermal emission component is seemingly negligible.

Key words. radio continuum: galaxies – galaxies: individual: NGC 3627 – ISM: molecules – stars: formation

1. Introduction

The star formation process powers the emissions of spiral galaxies across the whole electromagnetic spectrum. Star-forming galaxies are luminous sources of X-ray emission due to close accreting binaries with a compact companion, young supernova remnants, and hot plasma associated to star-forming regions and galactic winds (Fabbiano 1989). Young massive stars are strong sources of ultraviolet (UV) and, via the ionization of the interstellar medium (ISM), of H_α emissions (Rownd & Young 1999). The dust heated by the interstellar radiation field produces the far infrared (FIR) luminosity. At millimeter wavelengths the CO emission traces the bulk of molecular gas in which star formation occurs (e.g., Young & Scoville 1991), the HCN emission is also a reliable tracer of dense

molecular regions. The radio emission, at centimeter wavelengths, from galaxies consists of a mixture of non-thermal and thermal component, produced via synchrotron emission and free-free emission from HII regions, respectively. Correlations between global luminosities, integrated over the entire galaxies, at these different wavelengths have been reported by several authors. In particular, Ranalli et al. (2003) studied a X-ray/radio correlation in star-forming galaxies; Kennicutt (1998) established the global Schmidt law in galaxies using the correlation between IR and CO; Rownd & Young (1999) found a strong correlation between the H_α surface brightnesses and the CO integrated intensity; and, finally, a tight correlation between IR and HCN luminosities has been observed by Gao & Solomon (2004).

The tightest correlation observed in spiral galaxies is that between the non-thermal radio and the FIR luminosity (Condon 1992). This correlation extends over five decades and holds for a remarkably wide variety of galaxy types (e.g., Yun et al. 2001). It applies not only globally, but
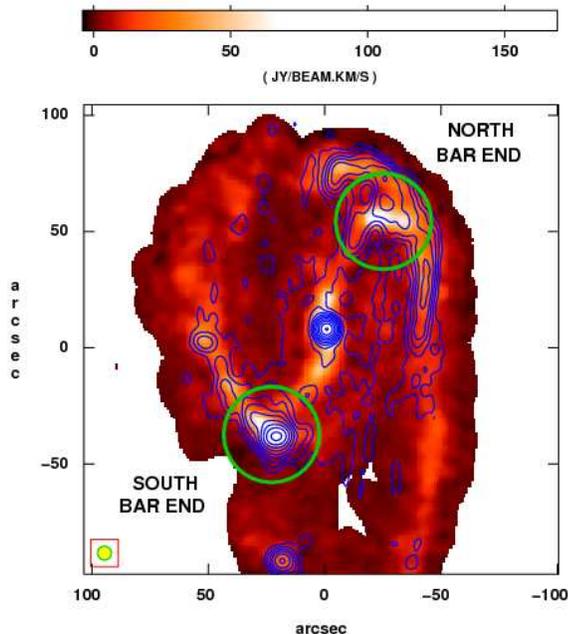
Fig. 1. Overlay of the VLA 1.4 GHz (contours) and BIMA CO (grey-scale) intensity. The synthesized beam of both observations (6″) is shown in lower left corner. The circles mark the north and south bar end regions we observed with the Plateau de Bure Interferometer and with VLA; their diameter represents the primary beam of a single PdBI antenna at 115 GHz.

also on kpc scales within the discs of individual galaxies (e.g., Boulanger & Perault 1988; Bicay & Helou 1990; Murphy et al. 2006a; Tabatabaei et al. 2007). It has been established also that the CO emission in spiral galaxies is well correlated with the radio-continuum (RC) emission on global and intermediate scales (e.g., Rickard et al. 1977; Israel & Rowan-Robinson 1984; Adler et al. 1991; Murgia et al. 2002). Recently, Murgia et al. (2005) and Paladino et al. (2006) extended the study of the RC-CO correlation down to angular scale of ∼ 6″ for a sample of 22 spiral galaxies selected from the Berkeley-Illinois-Maryland Association 3mm CO Survey of Nearby Galaxies (BIMA SONG; Regan et al. 2001; Helfer et al. 2003). They found that the RC-CO correlation is as tight as the global one, down to sub-kpc size scales.

Despite the fact that the aforementioned local RC and CO studies on galaxies enhance differences between the slopes of the correlation from galaxy to galaxy, and inside the same galaxy, from region to region, they clearly indicate that the RC brightness is spatially correlated to the CO emission. So far, the scarce angular resolution of the FIR observations prevents detailed investigations of the FIR-RC correlation on sub-arcminute scales. Nonetheless, recent high resolution *Spitzer* observations allow us the comparison of RC and CO emissions to shorter wavelengths than the FIR ones. In fact, using *Spitzer* 24 μm images, we found that RC is still correlated with this emission (Paladino et al. 2006). The question that we are try-

ing to address is, what are the physical basis of these spatial correlations. The non-thermal RC is, for the most part, synchrotron emission that arises from the interaction of relativistic electrons with the ambient magnetic field in which they diffuse. These electrons are supposed to be accelerated in supernova remnants, which represent the ultimate phase of the life of massive stars. The reason why RC emission is so closely related to IR and CO is not so straightforward. We know that the relativistic electrons diffuse from their birthplaces, therefore one would expect that the spatial correlations break down below the characteristic diffusion scale-length of the radiating electrons. A typical value of relativistic electrons diffusion scale in spiral galaxies is of the order of a few kpc (see also Sect. 4). Although, the value of the diffusion scale is extremely uncertain, depending on the propagation of cosmic-ray electrons along magnetic field lines, which is not fully understood.

The recent result of a tight RC-CO-24 μm correlations down to sub-kpc scale (Paladino et al. 2006) indicates either that we have not yet probed the spatial scale at which the correlations break down or that there is a mechanism of regulation that compensates the electrons diffusion. With the aim of testing the former possibility we present the results obtained on one galaxy of the studied sample (Paladino et al. 2006), NGC 3627, observed at resolution of ∼ 100 pc, by extending the study of the correlations between RC and CO emission to higher linear resolutions.

We present new RC and CO observations, at a resolution of 2″, of two regions of the spiral galaxy NGC 3627, obtained with the Very Large Array[1] (VLA) and the Plateau de Bure Interferometer (PdBI), respectively. The galaxy NGC 3627 is a promising target because it is a relatively nearby, face-on galaxy, at the distance of 11.1 Mpc (Saha et al. 1999). At this distance 1″ corresponds to 53 pc. Both RC and CO emissions are localized in a narrow bar structure of ∼300 pc in width. The emissions show a peak at the position of the nucleus, which extend along the leading edges of the bar forming two broad peaks at the bar ends, and then trail-off into the spiral arms. Paladino et al. (2006) found that 24 μm-RC-CO correlations in this galaxy persist down to a spatial scales of 350 pc. The new RC and CO observations are focused only on two regions of the bar far away from the nucleus of the galaxy (see Fig. 1). As NGC 3627 is a Seyfert galaxy, we prefer to avoid the core whose RC emission is likely contaminated by the active galactic nuclei.

We report on the outcomes of new RC and CO observations of two regions of NGC 3627, at resolution of ∼2″, corresponding to ∼ 100 pc at a distance of 11 Mpc. The resolution achieved is comparable to that of mid-IR *Spitzer* observations. In order to add information about the connection between the RC emission and other thermal emissions on spatial scale of 100 pc, we compare our new observations to archival 8, 5.8, 4.5 μm *Spitzer* and H$_\alpha$ observations. This work is organized as follows: in Sect. 2, we summarize new and archival observations, and give details of data reduction procedures. Data analysis and results are pre-
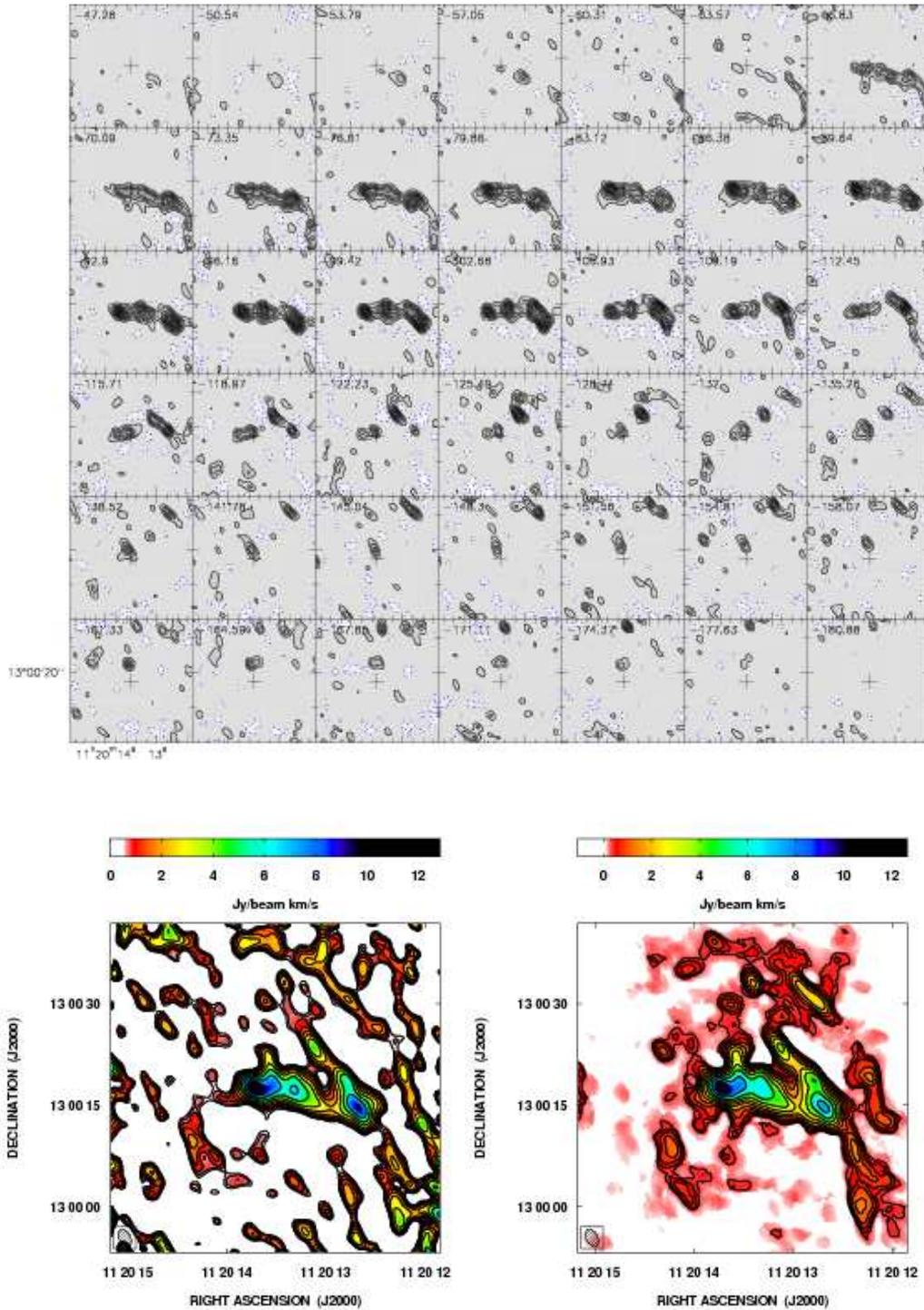
Fig. 2. North bar end of NGC 3627. *Upper panel*: ^{12}CO(1-0) velocity-channel maps observed with the PdBI. The angular resolution is of $2\rlap{.}''72 \times 1\rlap{.}''75$ at PA$=31^{\circ}$. We map an area of view of $35''$(the diameter of the primary beam at 115 GHz is of $43''$). The phase tracking center is indicated by a cross at $\alpha_{J2000}=11^{h}20^{m}13.5^{s}$ and $\delta_{J2000}=13^{\circ}00'17\rlap{.}''7$. Velocity-channels are displayed from v$=-47.28$ km s^{-1} to v$=-180.88$ km s^{-1} in steps of 3.26 km s^{-1}. Velocities are referred to the LSR and the zero velocity corresponds to $v_0=712.6$ km s^{-1}. Contour levels start from -30 mJy beam^{-1} in step of 30 mJy beam^{-1}. The rms noise is 6 mJy beam^{-1} and only regions whose brightness is larger than 5-σ are shown.
Lower panel: North bar end of NGC 3627: ^{12}CO(1-0) integrated intensity. The left panel shows the velocity integrated image. Contour levels start from 0.4 Jy km s^{-1} beam^{-1} (the 1-σ level is 0.13 Jy km s^{-1} beam^{-1}) and scale by a factor of $\sqrt{2}$. The right panel shows the image obtained using the smooth-and-mask technique (see Sect.2.1). The grey-scale image shows emissions larger than the pixel 3 σ level. The contours start from 0.3 Jy km s^{-1} beam^{-1}, an average value of the rms in fainter regions, and scale by a factor of $\sqrt{2}$.
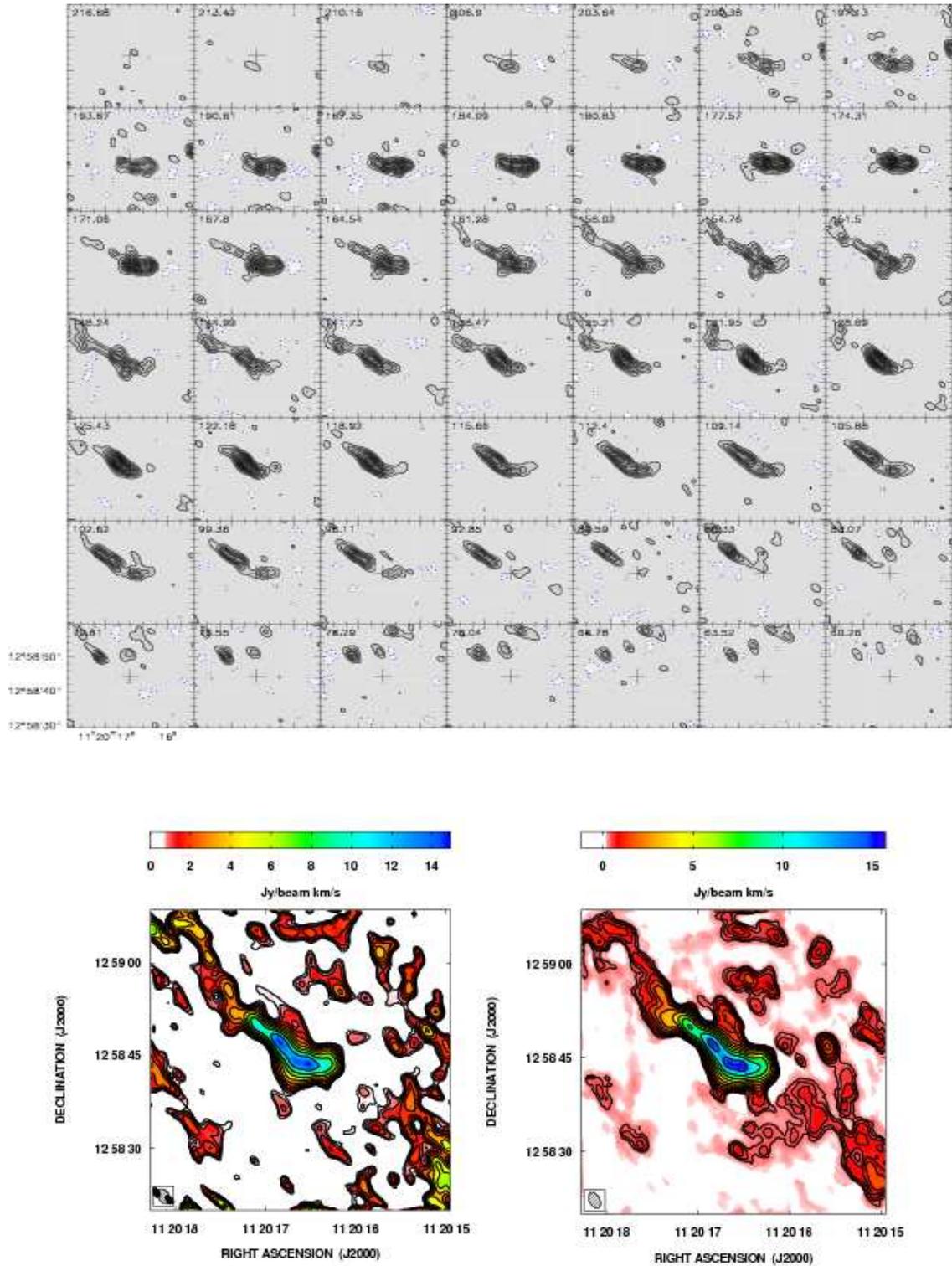
Fig. 3. South bar end of NGC 3627. *Upper panel*: ^{12}CO(1-0) velocity-channel maps observed with the PdBI. The angular resolution of 2″.75×1″.73 at PA=31°. We map an area of view of 25″, i.e., about half of the diameter of the primary beam at 115 GHz. The phase tracking center is indicated by a cross at $\alpha_{J2000}=11^h20^m16.6^s$ and $\delta_{J2000}=12°58'44''.5$. Velocity-channels are displayed from v=216.68 km s^{-1} to v=60.26 km s^{-1} in steps of 3.26 km s^{-1}. Velocities are referred to the LSR and the zero velocity corresponds to v_0=712.6 km s^{-1}. Contour levels start from -30 mJy beam^{-1} with step of 30 mJy beam^{-1}.The rms noise is 7 mJy beam^{-1} and only regions whose brightness is above 4-σ levels are shown.
Lower panel: ^{12}CO(1-0) integrated intensity. The left panel shows the velocity integrated image. Contour levels start from 0.5 Jy km s^{-1} beam^{-1} (the 1-σ level is 0.16 Jy km s^{-1} beam^{-1}) and scale by a factor of $\sqrt{2}$. The right panel shows the image obtained using the smooth-and-mask technique (see Sect. 2.1). The grey-scale image shows emission larger than the pixel 3-σ level. The

sented in Sect. 3. The results are discussed in Sect. 4, and a summary is given in Sect. 5.

2. Observations and Data Reduction

2.1. CO data

The observations of the CO emission from NGC 3627 were carried out with the IRAM interferometer on March 20, 2005, using the 6Cp configuration of the array. We observed simultaneously the J=1-0 and J=2-1 lines of ^{12}CO at the bar ends of the galaxy (for details see Fig. 1 and Tab. 1); the beam size is $2\rlap{.}''7 \times 1\rlap{.}''7$ and $1\rlap{.}''7 \times 0\rlap{.}''8$ in the CO(1-0) and CO(2-1) line, respectively.

The spectral correlator was split in two IF centered at 114.997 and 229.99 GHz, respectively. These are the transition rest frequencies of the two ^{12}CO lines for an assumed recession velocity of $v_0(LSR)=712.6$ km s^{-1}, which is the average of the recession velocities at the galaxy bar ends (Tab. 1). Using four partly overlapping 160 MHz-wide units, the correlator was configured to cover a bandwidth of 580 MHz for each line, corresponding to 1512 km s^{-1} and 756 km s^{-1} at 115 GHz and 230 GHz, respectively. We obtained visibilities with on-source integration times of 10 minutes framed by short ($\sim$ 2 min) integrations on the nearby quasars used as amplitude (3C84, 3C273) and phase (0923+392, 1055+018) calibrators. Total observing times are reported in table 2.

We are primarily interested in the CO(1-0) transition, and combine the PdBI data with the available BIMA observations. The ^{12}CO(2-1) observations are heavily affected by the "missing flux" problem (see Sect. 2.1.1), which makes them not reliable for a more quantitative analysis. However, for the sake of completeness, the CO(2-1) velocity channel maps and integrated intensity images are also reported in Appendix A.

In Figs. 2 and 3 (upper panels), we show the velocity channel maps observed with PdBI in the north and south bar ends, correspondingly. The rms derived from emission-free channels of 3.26 km s^{-1} is of 6 mJy beam^{-1} in the north bar end and of 7 mJy beam^{-1} in the south bar end. No continuum emission was detected, down to 1 σ rms noise level of 0.4 mJy beam^{-1} (0.5 mJy beam^{-1}), for the north (south) bar end.

In Figs. 2 and 3 (lower panels), we present the ^{12}CO integrated intensity images for the two observed regions. The left panel shows the integrated intensity obtained by summing all channels in the data cube. The 1-σ level is given by the noise estimated in the free channel multiplied by $\sqrt{N}\Delta v$, where N is the number of channels summed and the Δv is the width of each channel (3.26 km s^{-1}): in the north and south regions, the 1-σ levels are 0.13 Jy beam^{-1} km s^{-1} and 0.16 Jy beam^{-1} km s^{-1}, respectively. The right panel shows the integrated intensity formed using the smooth-and-masked technique (see Helfer et al. 2003), which is very effective in showing low level emission in the map. First, we smoothed the data cube by a Gaussian with FWHM=6″ and we created a mask accepting all pixels in each channel map where the signal was stronger than 3 σ rms noise level of the smoothed channel. Second, we selected in the full-resolution data cube only those pixels that with non-zero values in the mask file and summed them

| Source	RA	DEC	LSR Velocity
	(J2000.0)	(J2000.0)	(km/s)
NGC3627N	11:20:13.5	+13:00:17.7	+600
NGC3627S	11:20:16.6	+12:58:44.5	+825

Table 1. Pointing positions and local standard of rest velocities for the two bar ends.

|	VLA*	PdBI*	$\sigma_{1.4}$	$\sigma_{CO(1-0)}$
	hr	hr	μJy bm^{-1}	Jy bm^{-1} km s^{-1}
NGC3627N	6	8	22	0.13
NGC3627S	6	8	24	0.16

Table 2. Observations summary. Observing times and rms levels for VLA and PdBI observations (see Sect.2.1 and 2.2).

* Observing times include overheads.

to obtain the integrated intensity image. Finally, we multiplied the pixel values by the velocity width of an individual channel (3.26 km s^{-1}) to generate the image in the units of Jy beam^{-1} km s^{-1}. This technique implies a variation of the pixel-by-pixel rms in the CO integrated intensity image. The plots in Figs. 2 and 3 show contours starting from 0.3 Jy beam^{-1} km s^{-1}, the average value of the rms in fainter regions, whereas the grey-scale images show emissions above 3 times the rms measured pixel-by-pixel.
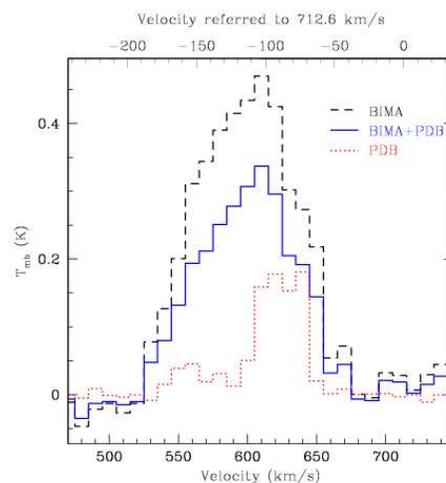
Fig. 4. Comparison of BIMA and PdBI spectra measured in the northern emission region. Data have been averaged in RA-DEC plane, obtaining the profile along the velocity axis. The PdBI spectrum is shown in (red) dotted line, the BIMA in (black) short dashed line and the short-spacing corrected spectrum in (blue) solid line.
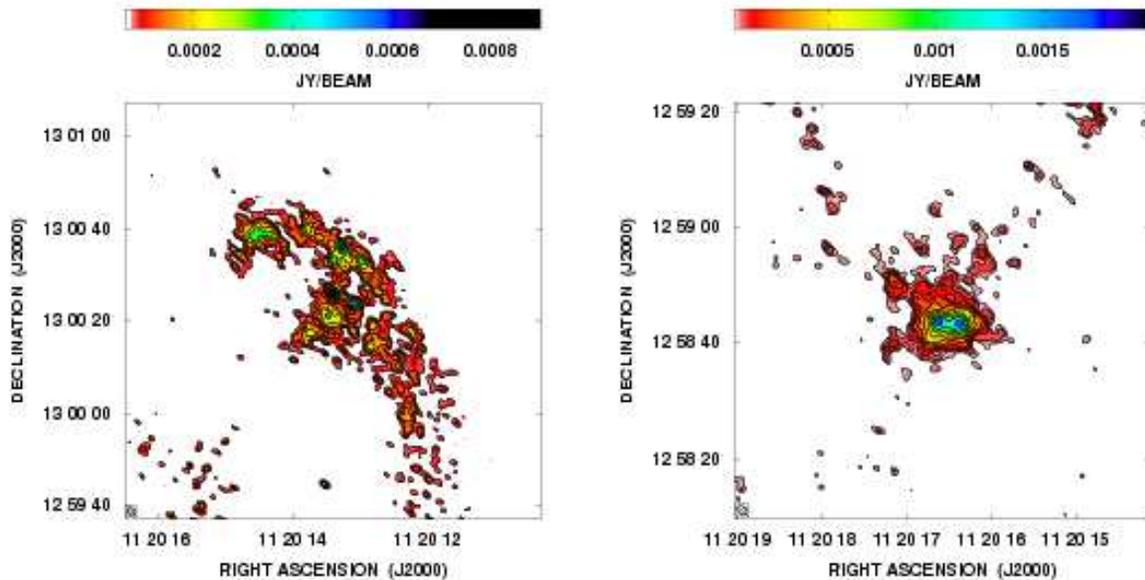
Fig. 5. VLA-A array images of north bar end (*Left*) and south bar end (*Right*) of NGC 3627. The angular resolution is of $1''9 \times 1''3$ at PA=49°. Contours level start from $72 \, \mu$Jy beam^{-1} and $66 \, \mu$Jy beam^{-1} (3σ), respectively, and scale by a factor of $\sqrt{2}$.

2.1.1. BIMA and PdBI data combination

Our PdBI observations are affected by the "missing flux" problem. The baselines range from 16 to 330 meters. The observed regions have extension of $\sim 25''$, larger than half the primary beam size of PdBI antennae at 115 GHz ($43''$). In this case, the PdBI observations may have missed about 50% of the flux (Helfer et al. 2002).

To reduce this problem we combined the PdBI data with those of the BIMA SONG. The BIMA interferometer has smaller antennas than PdBI (dish diameter is 6 m), and minimum dish separation of 8 m, the largest angular size detectable at 115 GHz being ~67''. In addition, data obtained with NRAO 12 m telescope have been incorporated to interferometric maps in BIMA SONG images, therefore these images are not missing any flux (Helfer et al. 2003). The combination should be performed by merging PdBI and BIMA u-v data together and then combining this with the 12 m data for the deconvolution (see Helfer et al. (2003) for the application of this method to the BIMA SONG). In our case, using this method is very difficult, since we have two discrete PdBI fields across a region containing extended emission observed in a multi-pointings mode with BIMA. We decided to combine PdBI and BIMA data in the image plane, using the technique implemented in the MIRIAD (Multichannel Image Reconstruction Image Analysis and Display) task IMMERGE (Sault et al. 1995). This technique requires caution, nevertheless, Wong & Blitz (2000) show that this method agrees well with the "linear combination" described in Stanimirovic et al. (1999) in which data are combined before deconvolution and then deconvolved with a composite beam. The task IMMERGE applies the "Fourier" technique: the maps are transformed to

the Fourier plane and merged together. In a specified annulus of the Fourier domain, where both images should agree, we calculated the flux calibration factor, which minimize differences between the data of the two resolutions. Since the ranges of baseline length of the PdB and BIMA interferometer are 20-230 m and 8-87 m, respectively, the annulus used is between 30 and 80 meters. Since the primary beams of the two images are different, the low-resolution image is tapered to match any residual primary beam response in the high-resolution one.

For the combination of PdB and BIMA data, we regrid the PdBI cubes to the same velocity grid as the BIMA+12m cubes. For comparison between the PdBI and BIMA data, in Fig. 4 we show the average spectrum measured in the northern region. Data have been averaged in RA-DEC plane, obtaining the profile along the velocity axis. In this plot it is evident that the inclusion of the short-spacing data has a noticeable impact on the flux of channels whose velocities lie between -120 and -180 km s^{-1}, i.e., those with more diffuse emission. Missing flux still remains an issue in our CO combined images. Nevertheless, we believe that the adopted combination technique is sufficient for our purpose of analyzing the moment-0 images. In particular, Helfer et al. (2003; their Fig. 53) indicate that the flux is uniformly lost by BIMA throughout the galaxy. Hence, if a similar behavior can be expected for our combined maps, the missing flux would only produce a horizontal shift of the point-to-point RC-CO correlations shown below (see Figs. 7 and 8), without affecting the slopes. Such an effect would not invalidate the overall results.
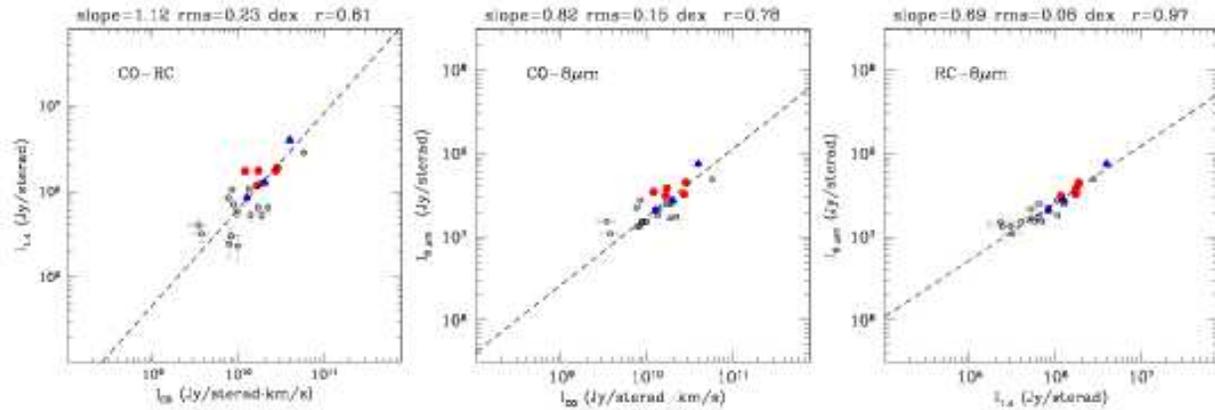
Fig. 6. Comparison between I$_{1.4}$, I$_{CO}$ and 8μm mid-IR emissions. Brightnesses are measured by averaging all pixel values within circles of 18″in diameter recovering the entire galaxy. Filled blue triangles represent the measures in the south bar end, filled red circles are those in the north bar end.

2.2. Radio continuum data

We observed the 1.4 GHz emission from the two regions of NGC 3627 with the VLA in its A configuration on April, 11, 2006, spending ~ 3.5 hours on each target . We observed with a bandwidth of 50 MHz for the two IF channels centered at 1.465 and 1.385 GHz.

The data were calibrated and imaged with the NRAO package AIPS following standard procedures: Fourier-Transform, Clean and Restore. Self-calibration was applied to minimize the effects of phase variations. The flux densities were brought to the scale of Baars et al. (1977) using the calibrators 3C138 and 3C286. The final cleaned maps were restored with beams of 1″9×1″3. Figure 5 shows the VLA-A array maps obtained for the two observed regions, produced using natural weighting. The final noise of total intensity images obtained for the north and south bar end region is of 22 and 24 μJy beam^{-1}, respectively.

To improve the sensitivity to large scale structures, the A-array data were combined with D and B-array data in the visibility plane, using the AIPS task DBCON. The B-array observations are described in Paladino et al. (2006), while those of the D-array are archival data. The combined image has a resolution of 2″07 × 1″43 and a rms level of 21 μJy beam^{-1}.

For the comparison with CO and IR images, we convolved the A+B+D-array VLA images to the beam of both BIMA and PdBI observations, i.e., 7″3 ×6″and 2″7 ×1″8, respectively. The derived low and high resolution images have a 1-σ noise of 136 μJy beam^{-1} and 27 μJy beam^{-1}, correspondingly.

2.3. Archival data

The spiral galaxy NGC 3627 has been observed as part of the *Spitzer* Infrared Nearby Galaxies Survey (SINGS Kennicutt et al. 2003), and IR *Spitzer* images. In addition, H$_\alpha$ images have been released in the context of the SINGS Second Data Delivery, April 2005.

The observations obtained with the Infrared Array Camera (IRAC; Fazio et al. 2004) at 4.5, 5.8, and 8 μm have resolutions of 1″2, 1″5, and 1″8, respectively. The Hα images, obtained at Kitt Peak National Observatory (KPNO) 2.1 m telescope, using a narrow-band filter centered at 6618 Å, have a PSF of 1″9. For details on *Spitzer* and Hα observations and data processing see delivery document for SINGS Second Data Delivery[2].

The resolution of IRAC and Hα images is only slightly smaller than that of our RC and CO images, making the comparison between these sets of images consistent. To this end, we convolved the IRAC and Hα images to the largest beam and performed the geometric transformation of images to match with the pointings of RC and CO observations.

We compare the RC and CO emission with the dust emission at mid-infrared wavelengths. The images at λ 24 μm can be considered pure 'dust' images, with negligible contributions from the photospheric emission of stars and from nebular emission, whereas the IRAC wavelenghts (3.6, 4.5, 5.8 and 8 μm) are dominated by stellar emission. In particular, the 4.5 μm emission is dominated by photospheric emission from stars, but can also contain a component of hot dust emission. In 5.8 and 8 μm images, however, the emission from PAH becomes significant. In order to obtain the distribution of dust at these wavelengths by subtracting the stellar contribution, we used the recipe of Helou et al. (2004). These authors assume that all the 3.6 μm emission is due to stars and extrapolate this component to longer wavelengths using stellar population modeling. To reproduce the star contribution at 4.5, 5.8, and 8 μm, Helou et al. (2004) scale the 3.6 μm map by 0.596, 0.399, and 0.232, respectively, and subtract these scaled maps from the observed maps pixel by pixel to yield the "dust maps". Since this method may underestimate the dust component e.g., the 3.6 μm images can contain a hot dust component in addition to photospheric emission we judge this approach as a reliable one for our pur-

---

[2] http://data.spitzer.caltech.edu/popular/sings/20050506_enhanced _v1/Documents/sings_second_delivery_v2.pdf
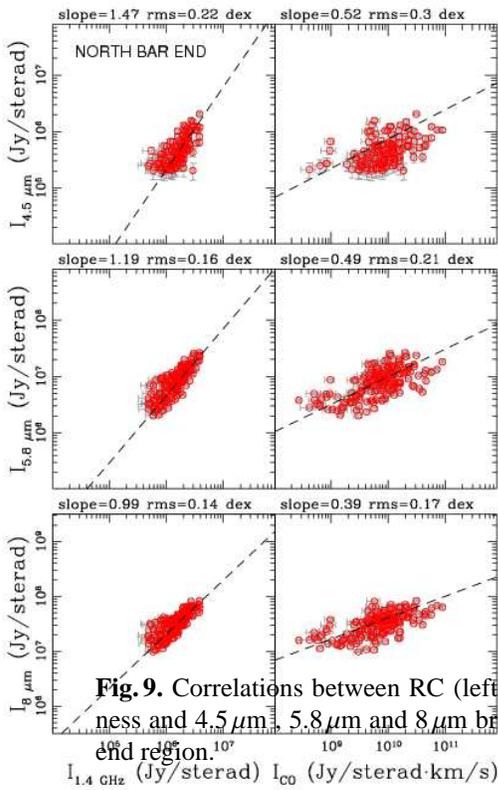
Fig. 9. Correlations between RC (left) and CO (right) ness and $4.5\,\mu$m , $5.8\,\mu$m and $8\,\mu$m brightness in the no end region.
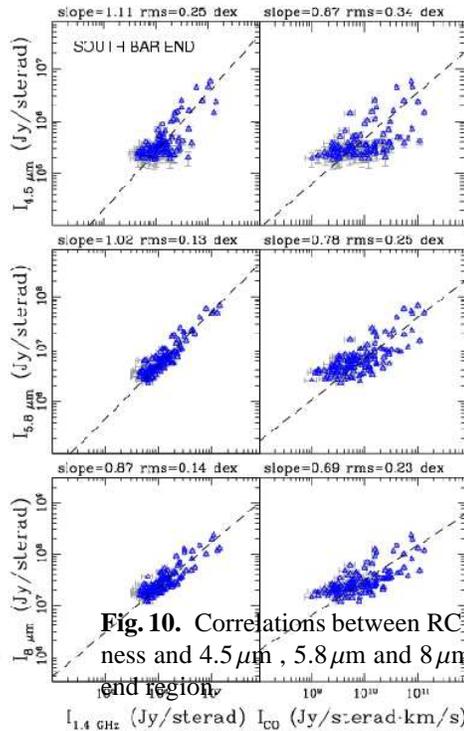
Fig. 10. Correlations between RC (left) and CO (right) brightness and $4.5\,\mu$m , $5.8\,\mu$m and $8\,\mu$m brightness in the south bar end region.

poses. In fact, the hot dust emission has an impact below few percent on the dust-only images (Calzetti et al. 2005).

3. Data analysis and results

We extend the study of the RC-CO-24 μm correlations obtained for a spatial scale of $6''$, reported in Paladino et al. (2006), to the $8\,\mu$m *Spitzer* data, convolving $8\,\mu$m images to the BIMA resolution: $7''.3 \times 6''$. To obtain a general view of the correlations across the entire galaxy, we overlaid a grid of circles with a diameter of $18''$ across the spiral structure. Then, we calculated the 1.4 GHz RC brightness ($I_{1.4}$), the CO integrated intensity (I_{CO}) and the mid-IR brightness ($I_{8\mu m}$) by averaging all pixel values within each circle. The correlations obtained are shown in Fig. 6. We fitted the observed data with a power law parametrized as $y(x) = c \cdot x^{slope}$, taking into account the errors of both x and y. The results of this fit and the Pearson coefficient of the correlations are reported as labels on the plots shown in Fig. 6. The correlations of the $8\,\mu$m emission with both RC

and CO have scatters 0.08 and 0.15 dex, respectively. This values are even lower than that of RC-CO correlation. In particular the RC-$8\,\mu$m correlation has a Pearson coefficient near 1. The slopes of the correlations are very different, depending on which variable is associated to the x and y-axis. To provide a more complete description of the RC-CO-$8\,\mu$m correlation, we introduce a three-dimensional view of it in Sect. 3.3.

In Figs. 6, points corresponding to northern and southern regions, observed at high resolution with the PdBI and the VLA in this work, are marked with filled blue triangles and filled red circles, respectively. In the following section, we report on the correlations studied at $2''$ resolution in these two regions.

3.1. The mid IR-RC-CO point-to-point correlation at $2''$

In order to compare point-to-point RC, CO, and mid-IR brightnesses in the observed regions, we overlaid on the images regular grids of rectangular boxes, whose dimensions coincide with the beam of observations (corresponding to a spatial scale of

x	y	North bar end			South bar end		
		slope	rms	r	slope	rms	r
I_{CO}	I_{RC}	0.43	0.17	0.56	0.77	0.21	0.84
I_{RC}	$I_{4.5\mu m}$	1.47	0.22	0.69	1.11	0.25	0.74
I_{RC}	$I_{5.8\mu m}$	1.19	0.16	0.85	1.02	0.13	0.95
I_{RC}	$I_{8\mu m}$	0.99	0.14	0.83	0.87	0.14	0.84
I_{CO}	$I_{4.5\mu m}$	0.52	0.3	0.41	0.87	0.34	0.53
I_{CO}	$I_{5.8\mu m}$	0.49	0.21	0.40	0.78	0.25	0.77
I_{CO}	$I_{8\mu m}$	0.39	0.17	0.52	0.69	0.23	0.67

Table 3. Coefficients of IR-RC-CO 2″correlations. Observed data have been fitted with the function $y(x) = c \cdot x^{slope}$. Slope is the result of the fit, rms is expressed in dex, and r is the Pearson's correlation coefficient.

100 pc), and we averaged all pixel values within each box. We performed the power law fitting described above, determining for each correlation the corresponding slope and normalization parameter. The results of this fit are reported as labels on the plots.

Figures 7 and 8 show the overlay of RC brightness contours on CO integrated intensity images and the plot of $I_{1.4}$ versus I_{CO} for both regions. The overlay of the emissions shows that CO and RC emissions distribute very similarly in both the north and south bar ends, despite the presence of minor local differences. In particular, both RC and CO emissions follow the same filamentary distribution in both regions. The plot of the point-to-point correlations show that in the north bar end the RC emission spans only one order of magnitude, whereas the CO emission varies over two orders of magnitude. In the south bar end instead, both RC and CO emissions vary by a comparable factor. This results in a flatter slope in the northern region (0.43) than in the southern one (0.77). The Pearson's correlation coefficient, r, is also different in the two regions (r=0.56 in the north bar end and r=0.84 in the south bar end), indicating that the RC is less correlated to the CO in the northern region than in the southern one. The scatter of both correlations (0.17 dex and 0.21 dex in the northern and southern region, respectively) is similar to that observed in the 6″ correlations presented in Paladino et al. (2006).

We performed the same point-to-point analysis using the 4.5, 5.8, and 8 μm "dust maps" (see Sect. 2.3), convolved to the same beam of RC and CO images. The results for north and south bar ends are reported in Figs. 9 and 10, respectively. In the two regions, it appears that both the RC and mid-IR emissions vary by about one order of magnitude, whereas the CO varies over almost three orders of magnitude, producing flat CO-mid IR correlations. The RC is well correlated with dust emissions of both 5.8 and 8 μm: the resulting correlations are nearly linear and scatters vary from 0.16 to 0.13 dex. The RC-4.5 μm correlation has a higher scatter, in particular in the southern region. We report, in Table 3, the fitted slopes, rms of the 2″ correlations, and the Pearson's coefficients.

3.2. The comparison with Hα images and the determination of thermal radio flux

The two regions of NGC 3627 show very different stellar and dust distributions. Some works report on observations of HII regions in this galaxy (see Hodge 1974 and Chemin et al. 2003). In the north bar end, crowded with stellar objects, dust and HII regions have been the subject of various works focused on supernovae SN1989B and SN1973R hosted in NGC 3627 (e.g., Van Dyk et al. 1999, Wells et al. 1994).

Figure 11 shows the comparison between the RC and CO emissions (contours) and the positions of brightest HII regions (crosses), as reported in Hodge (1974). Some distinct sources of RC emission lie over the positions of HII regions. Without a radio spectral index to verify the thermal nature of the radiation from these sources, we can only tentatively identify the radio emission as originating in the HII regions. Indeed, superposing the north bar end RC and Hα images, we found that the spatial distribution of the brightest Hα knots is well matched by the RC peaks of emission. Instead, the CO emission is located on the edges of HII regions, tracing the dust arc-like distribution.

In the south bar end region the RC and CO emissions show an extended distribution similar to that of dust, without resolved peaks of emission. In the Hα image, there are some distinct bright knots also identified by Hodge (1974) as HII regions, but they do not have a point-like RC-counterpart.

We used the H_α image to estimate the RC thermal component to evaluate its effect on the correlations. The typical thermal fraction of radio emission at 1 GHz, measured from integrated spectra of spiral galaxies is of the order of 0.10. In particular, for NGC 3627, Niklas et al. 1997 determined a thermal fraction < 0.09. We estimated the thermal radio flux from the emission in the Hα recombination line (see, e.g., Caplan & Deharveng 1986 and Niklas et al. 1997), using the Niklas et al. (1997) Eq. 2 in the following way:

$$\left(\frac{S_{th}}{mJy}\right) = 2.238 \cdot 10^9 \cdot \left(\frac{S_{H\alpha}}{erg\ s^{-1}\ cm^{-2}}\right) \cdot \left(\frac{T_e}{K}\right)^{0.42}$$
$$\times \left\{ ln[\frac{0.04995}{\nu/GHz}] + 1.5 \cdot ln\left(\frac{T_e}{K}\right) \right\} \qquad (1)$$

where S_{th} is the thermal radio flux density at frequency ν=1.4 GHz, assuming a thermal electron temperature T_e of 10^4 K and measuring the Hα flux: $S_{H\alpha}$. The mean value of the thermal flux, measured in the same grid of point-to-point analysis in the northern region, is 0.02 mJy. This value rises to 0.08 mJy in correspondence with the brightest HII regions (**??**, indicated as bold-face crosses in Fig. 11). In the northern region, we found that the thermal fraction ranges from 0.07 to 0.11. Even if our measure underestimates the thermal emission, owing to absorption of the Hα emission by dust, it is still likely sufficient for the purpose of roughly estimating the thermal flux density and to ensure that the thermal contribution to the radio emission on the spatial scales analyzed is of order of 10%, not significantly different from that measured on integrated spectra (Niklas et al. 1997).

name	24 μm-RC-CO			8 μm-RC-CO		
	ϕ	θ	rms	ϕ	θ	rms
			6″correlations			
NGC 3351	0.94	0.61	0.16	0.77	0.69	0.13
NGC 3521	0.77	0.35	0.14	0.57	0.39	0.11
NGC 3627	**0.95**	**0.60**	**0.23**	**0.63**	**0.75**	**0.19**
NGC 4826	0.92	0.74	0.15	0.76	0.82	0.14
NGC 5194	0.97	0.52	0.23	0.81	0.60	0.20
NGC 7331	0.87	0.36	0.10	0.73	0.38	0.09
All	0.92	0.60	0.25	0.65	0.72	0.24
			2″correlations			
NGC 3627 N				**0.32**	**0.32**	**0.19**
NGC 3627 S				**0.58**	**0.62**	**0.23**

Table 4. 3D fit coefficients. Observed data have been fitted with a line in three-dimensional space. θ and ϕ are the direction angles of the line, rms is the scatter of the data.

3.3. The 3D view

The RC-CO-IR correlations are usually studied separately as projection in different planes. What we observe is indeed a correlation between all three emissions. This three-dimensional aspect cannot show up in the usual 2-dimensional description. Hence, we present a new perspective, a three-dimensional representation, with which to visualize and study the RC-CO-IR correlation. We performed a fit to the data in a three-dimensional space, placing $\log(I_{CO})$, $\log(I_{IR})$, and $\log(I_{RC})$ in the x, y and z axis, respectively. We computed the line fitting of the observed points, by minimizing the distance of these points from the line:

$$\begin{cases} x = x_0 + \rho \cdot cos\theta \, cos\phi \\ y = y_0 + \rho \cdot cos\theta \, sin\phi \\ z = z_0 + \rho \cdot sin\theta \end{cases}$$

where (x_0, y_0, z_0) is a generic point through which the line passes, θ and ϕ are its direction angles, and ρ is a parameter. As the fit procedures are completely different, the 3D fit coefficients cannot be easily related to the power law indexes found for the two-dimensional correlations. However, our purpose is to introduce a promising technique to visualize the "unified" correlation between the three emissions. The extension of this representation to a larger sample of galaxies could possibly give insight into the physical explanation of the correlation itself.

We used the six galaxies studied in Paladino et al. (2006) as a reference sample for the three-dimensional correlation. Figure 12 shows the RC-CO-24 μm, with the plotted line representing the fit to all the data. We conducted the same analysis on RC-CO-8 μm correlation, but for the sake of conciseness, this figure is not shown. Values for the angles θ and ϕ, and the rms, resulting from the fit, for each galaxy are reported in Table 4.

In these correlations, we deal with surface brightnesses, and thus they are unaffected by distance biases. The scatter of the global 3-D correlation is of 0.24 dex, i.e., a factor 1.7. This is

the scatter among different galaxies, whereas the scatter within each galaxy is even smaller (see Table 4).

Figure 13 shows the comparison between the three-dimensional 2″ RC-CO-8 μm correlation in the two observed regions and the 6″ correlation on the entire galaxy. Red boxes and blue triangles represent measures obtained in the north and south bar ends, respectively. The fitted lines for each set of data are also plotted. The bold line is the result of the fit to the data of the entire galaxy at 6″. The line fitting data of the south bar end region presents direction angles similar to those of the entire galaxy, and resembling to those of all galaxies. On the contrary, the line fitting the northern region data has lower direction angles, indicating a flatter correlation.

4. Discussion

Studying the RC, CO, and 8 μm emissions from two regions of spiral galaxy NGC 3627, we found that, despite some minor local variations, the spatial distributions of RC, CO, and 8 μm emissions match very well. The phenomenological model (see Bicay & Helou, 1990 and, more recently, Murphy et al., 2006b) proposed that the radio images should be a smoothed version of the IR maps due to the diffusion of cosmic-ray electrons from the star-forming regions. The results obtained in our study may suggest a more complex picture.

The propagation of cosmic rays along magnetic field lines is, however, still matter of debate. It is generally recognized that the cosmic rays propagating along the galactic magnetic field are continuously scattered and accelerated (see Melrose, 1968). Since the late 1970's, the proposed theory of diffusive shock acceleration has been developed and widely accepted. This theory proposes the statistical Fermi's acceleration mechanism as the responsible for the particles acceleration (Fermi 1949) and charges the slowing of such particles with reflections at strong shock waves. Without going into detail (see Strong et al. 2007, for a recent review on the cosmic ray propagation and interactions in the Galaxy) we can say that the bulk propagation of cosmic rays is slowed down to the velocity of magneto-hydrodynamic (MHD) waves, which is the Alfvén speed, $v_A = \sqrt{B^2/8\pi\rho} = 1.6 \cdot 10^5 \, n^{-1/2} \, B_{\mu G}$, in cm s^{-1}, where B is the magnetic field strength, and ρ and n are the density and number density of the gas, respectively. For a typical disk magnetic field strength B~ 5 μG (Condon 1992) and a density of the warm phase of the galactic disk ISM (which may be responsible for turbulent diffusion of cosmic rays) n=0.3 cm^{-3} (Biskamp 2003), the Alfvén velocity is ~15 km s^{-1}. The synchrotron lifetime τ, at ν_c=1 GHz, is of about 10^8 yrs. In these conditions, the diffusion scale-length of the radiating electrons, $L_{diff} \sim v_A \cdot \tau$, is of 1.5 kpc.

The scale we have examined (100 pc) is much lower than the electron diffusion scale. Nevertheless, in the two observed regions the RC emission does not appear to be more diffuse than that of CO and 8 μm. We compare the relative shapes of the emission profiles taking a one-dimensional slice of the RC, CO, and IR images. Due to the clumpy distribution of the emissions at this resolution, the profiles obtained along some paths contain multiple emission maxima corresponding to resolved features. In Fig. 14, the profiles obtained along two slices in
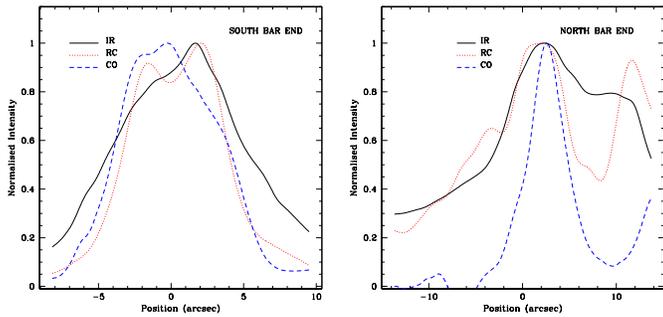
Fig. 14. Emission profiles of RC, CO and IR. *Left panel*: Profiles along the horizontal direction in the south bar end region. *Right panel*: Profiles along a slice in the thin arm. See Fig. 11 for the slice position.

the observed regions (the positions of slices are shown as black lines in Fig. 11) are reported as an example. The IR, RC, and CO profiles have been plotted with normalized peak amplitude to facilitate a comparison of their shapes and their spatial co-incidence. The slice in the southern region is taken along the horizontal direction. The RC and CO widths are comparable and not greater, as possibly expected, than the analogous width of the dust emission at $8\,\mu$m. For the northern region we report the profiles taken along a slice in the thin arm structure, where all the three emission are detected. In this case the most concentrated emission appears to be the CO one, while the RC emission profile does not appear to be a smoothed version of the IR one. In both regions, there is evidence that RC emission is not more diffuse than the CO and $8\,\mu$m emission. This is a surprising result, as the observed regions are much smaller than the expected electron diffusion scale.

It is important to stress that we found that the RC emission is well correlated to the emissions at μ m wavelengths in the northern and southern region. The μm emission traces a different dust component than that traced by the FIR emission. In practic, while the latter represents cold dust, as mentioned before, the $4.5\,\mu$m emission contains component of hot dust, whereas in 5.8 and $8\,\mu$m images the emission from PAH becomes significant. The CO emission varies over three order of magnitude while dust emission spans only one order of magnitude. In our opinion, this result could be explained considering that the CO emission traces molecular gas where star formation may just begin, whereas the bulk of the $8\,\mu$m emission, for example, comes from PAH molecules and these particles are in turn concentrated near regions of current star formation.

As we noted in previous sections, the north bar end region presents flat correlations of CO emission with both RC and IR. The flat RC-CO slope can be produced either by an higher RC brightness or a lower CO integrated intensity with respect to the average RC-CO relation. Assuming that the excess of RC brightness is due to the RC thermal component, the thermal fraction would be of 0.55. This value is higher than what we measure from the H_α emission (see Sect. 3.2), and thus this hypothesis is unlikely. Otherwise, if the CO is lower than average, a possible explanation can be the photo-destruction of molecular clouds near HII regions by ultraviolet photons (for a review

on photo-dissociation regions see, e.g., Hollenbach & Tielens 1999). This option can explain the lack of CO emission in correspondence with bright HII regions with RC counterpart, nevertheless it still need to be quantitatively verified. Certainly, more complex mechanisms are taking place in the observed regions, especially since the ends of the bar might suffer from turbulent motions that influence the velocity field.

Since the RC brightness critically depends on the galaxy's magnetic field B and cosmic-ray electron distribution N_0, and the separation between these two contributions is not yet clear, the interpretation of the results obtained is difficult. Spatially resolved spectral index studies at low frequencies, where the thermal emission component is seemingly negligible, can help to clarify the situation.

5. Summary and concluding remarks

We studied the correlations between the 1.4 GHz radio continuum, the CO, and the IR emission at short-wavelengths in two regions of the spiral galaxy NGC 3627. We carried out new VLA and PdBI observations down to an angular resolution of order of $2''$, which corresponds to a resolution of ~ 100 pc at the distance of 11 Mpc. We used the released IRAC and Hα SINGS images of comparable resolution. Even if the scale we examined is much lower than the electron diffusion scale we do not find evidence of a diffusion of the RC emission with respect to the scales of CO and $8\,\mu$m, as would be expected by previous phenomenological models.

The observed regions are located at the northern and southern ends of the bar of NGC 3627 where two broad peaks of emission are shown both in RC and CO images. Our new high resolution observations permit a distinction between compact and extended emission that would not be possible with previous data. In particular, in the northern region we can resolve some RC peaks have a spatial coincidence with HII knots.

We point out that our results refer to one single object, and, in particular, to two distinct regions in this object, and we do not attempt to provide a definite answer to the question. Our main result is that in these two regions, even at scales of 100 pc, where we would expect a break down of the correlations due to the cosmic rays diffusion, the RC emission is still correlated to that of CO. Furthermore we found that the RC emission is also correlated to the 4.5, 5.8 and $8\,\mu$m dust emission. Whatever these emissions trace, their correlation with RC emission on such a small scales is surprising and requires explanation. The study of a significant sample of galaxies would answer some of the questions left open.

Interestingly, in the northern region the RC-CO and IR-CO correlations have flatter slopes with respect to the average correlations, which might be due, among other options, to the photo-dissociation of molecular clouds near HII regions. Despite this minor deviation, the spatial distributions of RC follows well those of CO and IR, tracing thin arc-like structures. The widths of several structures, measured along slices across them, are similar in the RC, CO, and $8\,\mu$m maps. This indicates that the scale of RC emission is not larger than those of $8\,\mu$m and CO.

Furthermore, to give a complete description of the RC-CO, CO-mid IR, and RC-mid IR correlations, we have proposed a more concise and effective three-dimensional representation of the correlation, producing a three-dimensional fit of the observed data. We found that RC, CO, and mid-IR observed data are fitted by a line in three-dimensional space with a scatter of about 0.25 dex. In our opinion, this is a promising technique to visualize the "unified" correlation between the three emissions.

This study is focused on two individual regions of the galaxy NGC 3627, and the analysis of more objects has certainly to be done. Nevertheless, the observed correlation between RC, CO, and mid-IR emissions down to spatial scale of 100 pc may suggest that the coupling between electrons diffusion, losses, and injection is far more complex than expected. Future works on spectral index at high resolution will help to separate the contributions to the RC brightness due to the strength of magnetic field from that due to the density of relativistic electrons.

Appendix A. CO(2-1) observations

Figures 15 and 16 show the ^{12}CO(2-1) velocity-channel maps and the integrated intensity observed with the PdBI in the north and south bar end regions, respectively.

The ^{12}CO(2-1) and ^{12}CO(1-0) emissions are detected in almost the same velocity range. The 230 GHz channels have been compressed to have the velocity resolution of 3.26 Km s^{-1}.

Due to the particularly severe missing flux problem in these images, they are not reliable for quantitative studies. Nevertheless, we note that the northern ^{12}CO(2-1) emission has a peak coincident with the ^{12}CO(1-0) peak, and that in the southern region three different peaks of emission are resolved (Figure 16).
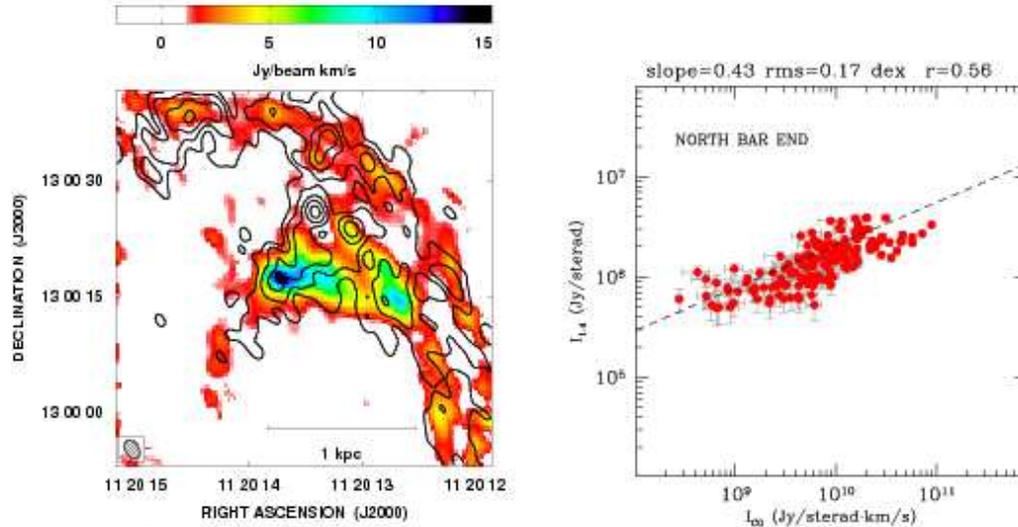
References

Adler, D. S., Allen, R. J., & Lo, K. Y. 1991, ApJ, 382, 475

Baars, J. W. M., Genzel, R., Pauliny-Toth, I. I. K., & Witzel, A. 1977, A&A, 61, 99

Bicay, M. D. & Helou, G. 1990, ApJ, 362, 59

Biskamp, D. 2003, Magnetohydrodynamic Turbulence (Magnetohydrodynamic Turbulence, by Dieter Biskamp, pp. 310, Cambridge University Press, September 2003.)

Boulanger, F. & Perault, M. 1988, ApJ, 330, 964

Calzetti, D., Kennicutt, R. C., Bianchi, L., et al. 2005, ApJ, 633, 871

Caplan, J. & Deharveng, L. 1986, A&A, 155, 297

Chemin, L., Cayatte, V., Balkowski, C., et al. 2003, A&A, 405, 89

Condon, J. J. 1992, ARA&A, 30, 575

Fabbiano, G. 1989, ARA&A, 27, 87

Fazio, G. G., Hora, J. L., Allen, L. E., et al. 2004, ApJS, 154, 10

Fermi, E. 1949, Physical Review, 75, 1169

Gao, Y. & Solomon, P. M. 2004, ApJS, 152, 63

Helfer, T. T., Thornley, M. D., Regan, M. W., et al. 2003, ApJS, 145, 259

Helfer, T. T., Vogel, S. N., Lugten, J. B., & Teuben, P. J. 2002, PASP, 114, 350

Helou, G., Roussel, H., Appleton, P., et al. 2004, ApJS, 154, 253

Hodge, P. W. 1974, ApJS, 27, 113

Hollenbach, D. J. & Tielens, A. G. G. M. 1999, Rev. Mod. Phys., 71, 173

Israel, F. & Rowan-Robinson, M. 1984, ApJ, 283, 81

Kennicutt, R. C. 1998, ApJ, 498, 541

Kennicutt, Jr., R. C., Armus, L., Bendo, G., et al. 2003, PASP, 115, 928

Melrose, D. B. 1968, Ap&SS, 2, 171

Murgia, M., Crapsi, A., Moscadelli, L., & Gregorini, L. 2002, A&A, 385, 412

Murgia, M., Helfer, T. T., Ekers, R., et al. 2005, A&A, 437, 389

Murphy, E. J., Braun, R., Helou, G., et al. 2006a, ApJ, 638, 157

Murphy, E. J., Helou, G., Braun, R., et al. 2006b, ApJ, 651, L111

Niklas, S., Klein, U., & Wielebinski, R. 1997, A&A, 322, 19

Paladino, R., Murgia, M., Helfer, T. T., et al. 2006, A&A, 456, 847

Ranalli, P., Comastri, A., & Setti, G. 2003, A&A, 399, 39

Regan, M. W., Thornley, M. D., Helfer, T. T., et al. 2001, ApJ, 561, 218

Rickard, L. J., Turner, B. E., & Palmer, P. 1977, ApJ, 218, L51

Rownd, B. K. & Young, J. S. 1999, AJ, 118, 670

Saha, A., Sandage, A., Tammann, G. A., et al. 1999, ApJ, 522, 802

Sault, R. J., Teuben, P. J., & Wright, M. C. H. 1995, in ASP Conf. Ser. 77: Astronomical Data Analysis Software and Systems IV, 433

Stanimirovic, S., Staveley-Smith, L., Dickey, J. M., Sault, R. J., & Snowden, S. L. 1999, MNRAS, 302, 417

Strong, A. W., Moskalenko, I. V., & Ptuskin, V. S. 2007, Annual Review of Nuclear and Particle Science, 57, 285

Tabatabaei, F. S., Beck, R., Krause, M., et al. 2007, A&A, 466, 509

Van Dyk, S. D., Peng, C. Y., Barth, A. J., & Filippenko, A. V. 1999, AJ, 118, 2331

Wells, L. A., Phillips, M. M., Suntzeff, B., et al. 1994, AJ, 108, 2233

Wong, T. & Blitz, L. 2000, ApJ, 540, 771

Young, J. S. & Scoville, N. Z. 1991, ARA&A, 29, 581

Yun, M. S., Reddy, N. A., & Condon, J. J. 2001, ApJ, 554, 803

List of Objects

Fig. 7. *Left*: Overlay of RC brightness (contours) on CO integrated intensity (grey-scale image) for the north bar region observed at a resolution of $2\rlap{.}''74\times1\rlap{.}''76$. Contours level start from 0.2 mJy beam^{-1} (5σ) and scale by a factor of $\sqrt{2}$. Note that the spatial coincidence between the two emissions is maintained well below the kpc scale. *Right*: $I_{1.4}$ versus I_{CO}. Brightnesses are measured by averaging all pixel values within beam-sized boxes recovering the entire region of emission. Only points above $3\,\sigma$ level have been plotted.
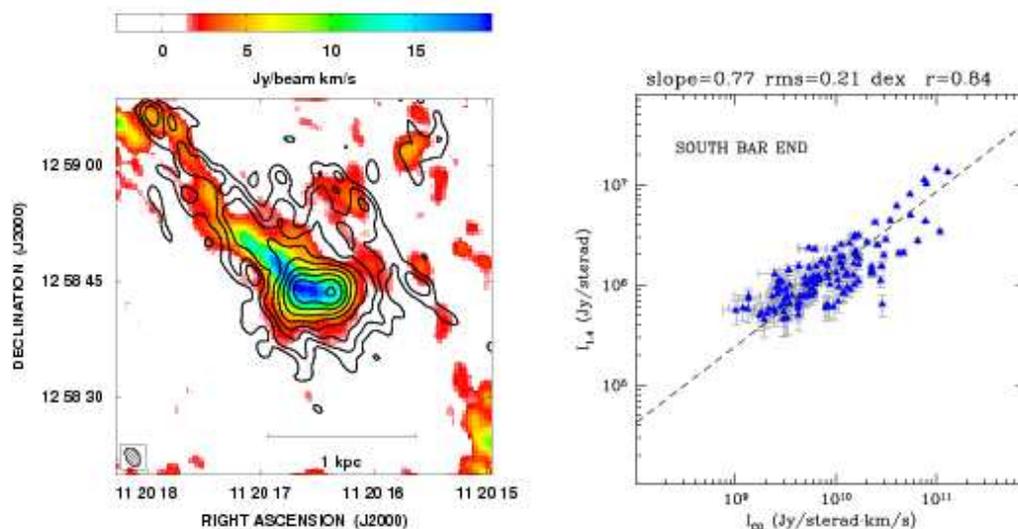

Fig. 8. *Left*: Overlay of RC brightness (contours) on CO integrated intensity (grey-scale image) for the south bar region observed at resolution of $2\rlap{.}''74\times1\rlap{.}''76$. Contours level start from 0.15 mJy beam^{-1} (5σ) and scale by a factor of $\sqrt{2}$. Note that the spatial coincidence between the two emissions is maintained well below the kpc scale. *Right*: $I_{1.4}$ versus I_{CO}. Brightnesses are measured by averaging all pixel values within beam-sized boxes recovering entire region of emission. Only points above $3\,\sigma$ level have been plotted.
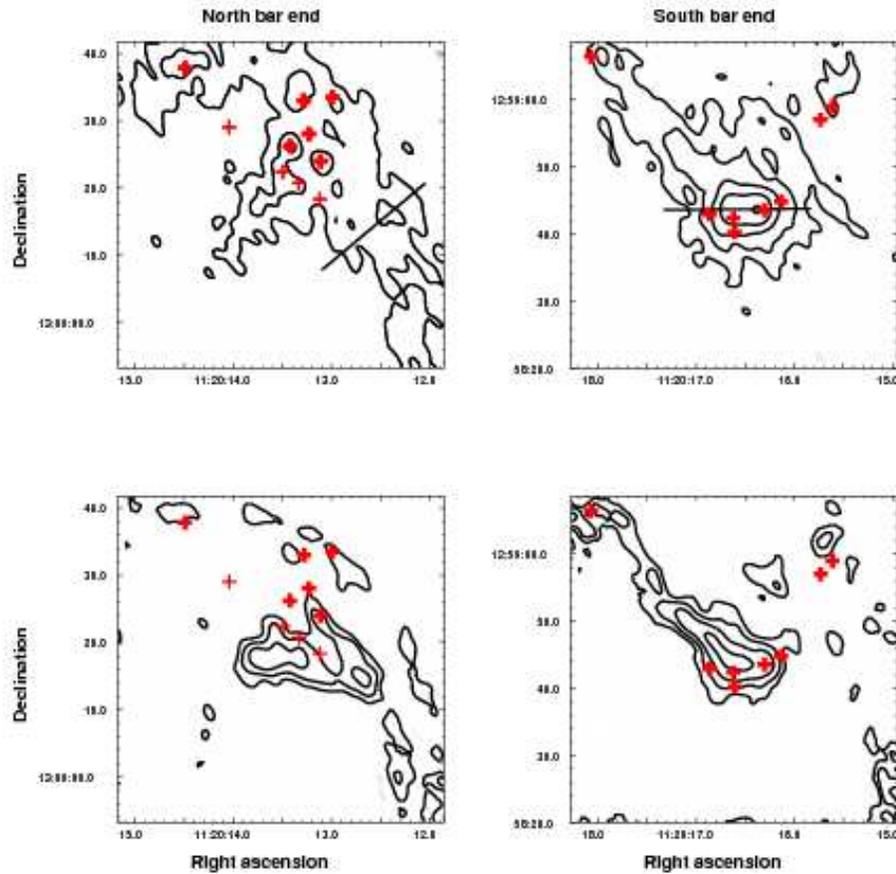
Fig. 11. Comparison between radio continuum (upper panels) and CO (lower panels) maps with HII regions positions. RC and CO contours start from 0.2 mJy beam^{-1} and 2 Jy beam^{-1} km s^{-1}, respectively, and scale by a factor of 2, to enhance point sources. Red crosses represent positions of brightest HII regions in the north (left panels) end, south (right panel) bar end. For a complete list of HII regions in NGC 3627, see Hodge (1974). Black lines in upper panels show the positions of two slices for the comparison of emission profiles (see Sect. 4).
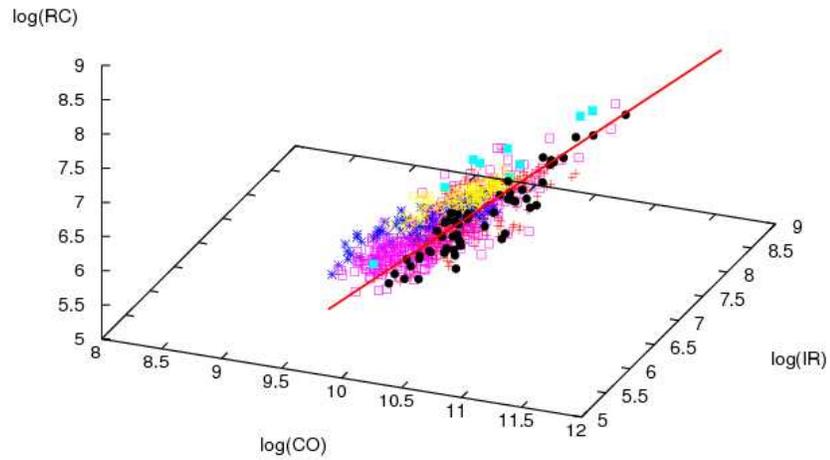
Fig. 12. RC, CO, and 24 μm 3D correlation. The x, y, and z axis are the log(CO), log(IR) (24 μm), and log(RC), respectively. Data at 6″ resolution of six galaxies reported in Table 4 are shown and the line plotted is the result of the fit for all data. The scatter of this fit is 0.25 dex.
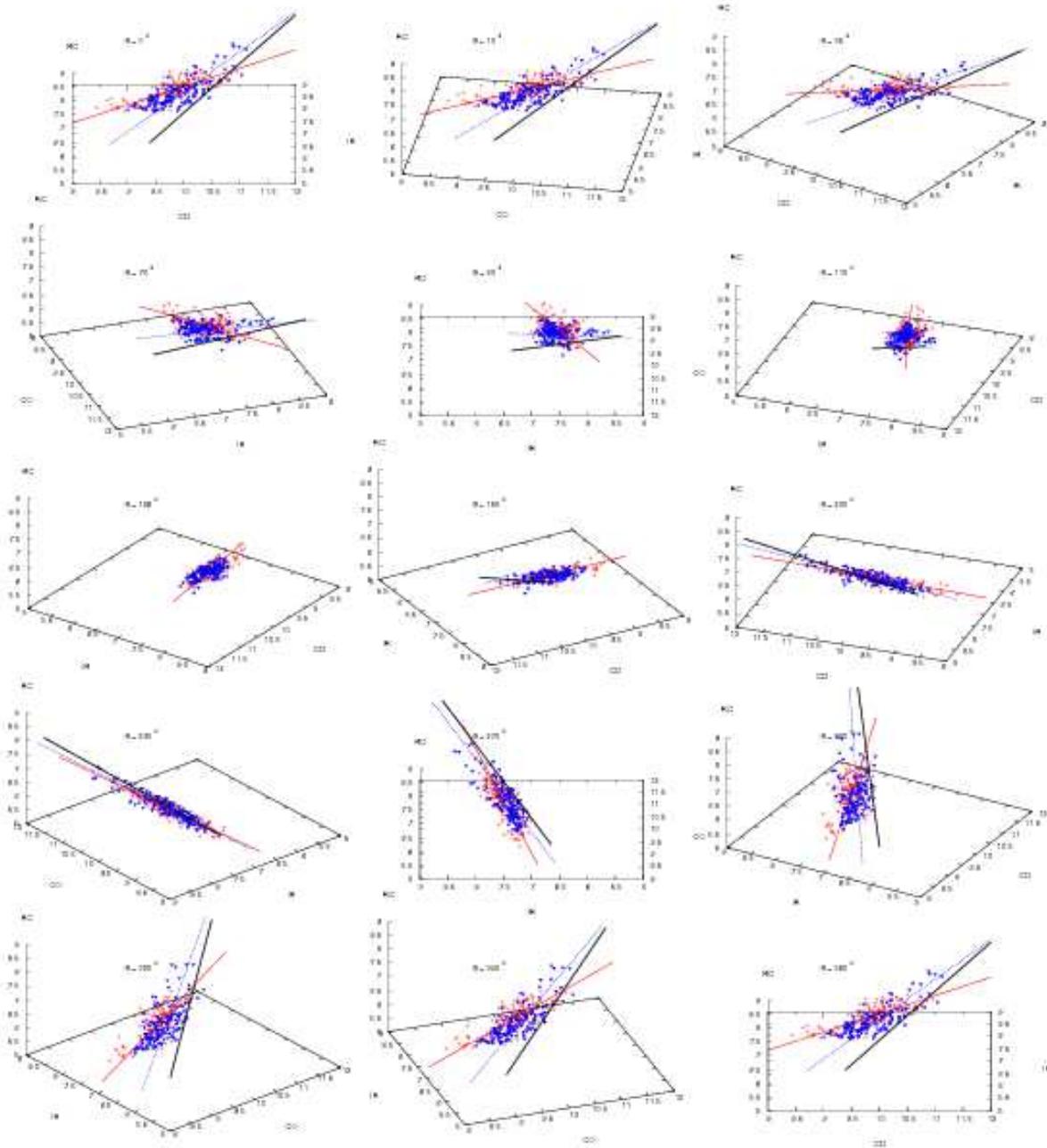
Fig. 13. RC, CO and 8 μm 3D correlation at 2″. The x, y, and z axis are log(CO), log(IR) (8 μm), and log(RC), respectively. Data at $\sim$ 2″ resolution of northern and southern region of NGC 3627 are represented by red crosses and blue triangles, respectively. Red solid and blue dotted lines represent the fit of these two set of data. The bolded black line corresponds to the fit of 6″RC, CO, and 8 μm data of the overall galaxy NGC 3627.
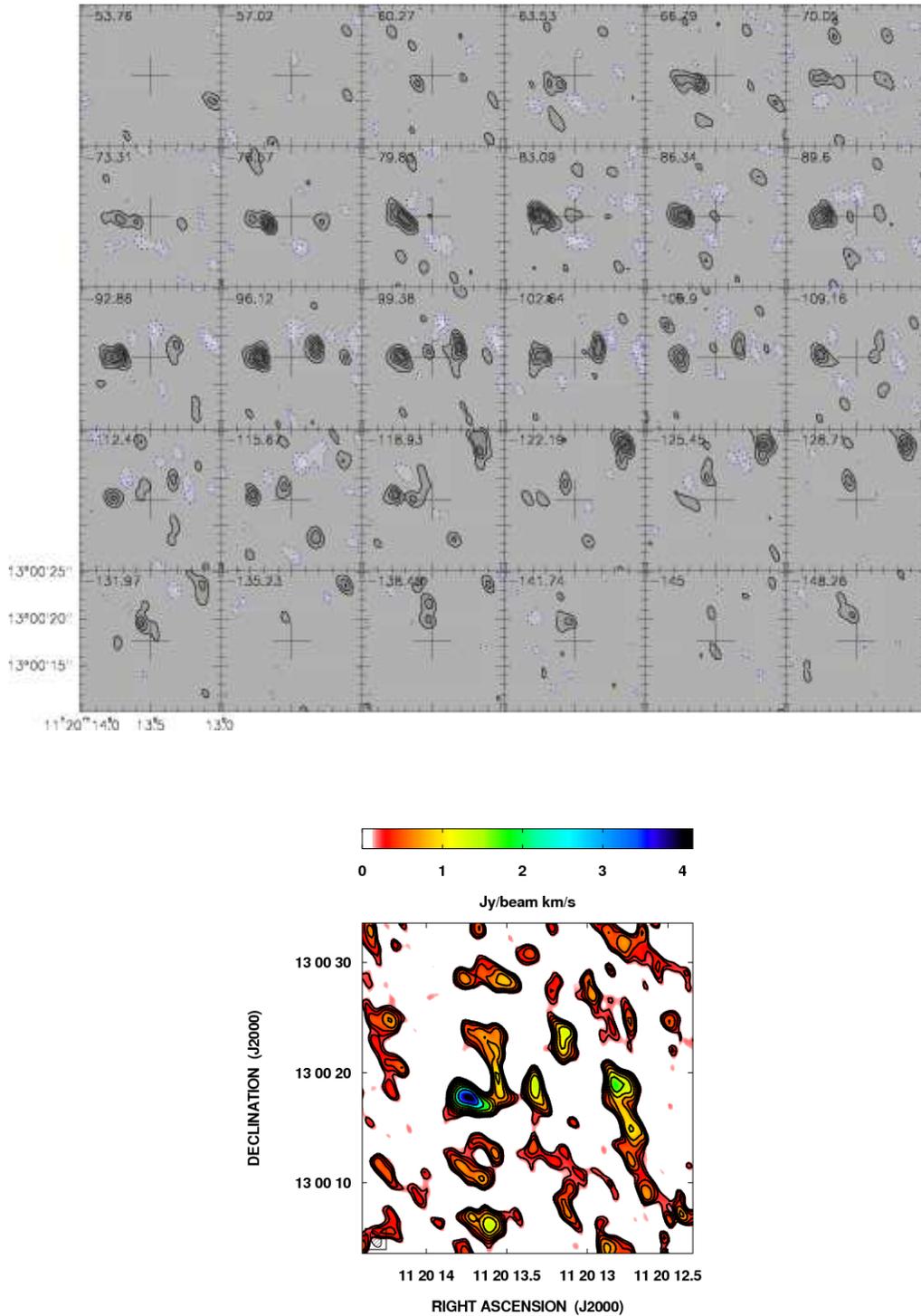
Fig. 15. North bar end of NGC 3627. *Upper panel*: ^{12}CO(2-1) velocity-channel maps observed with the PdBI. The spatial resolution is of $1\rlap{.}''59 \times 0\rlap{.}''88$ at PA=22°. We map an area of view of 15″. The phase tracking center is indicated by a cross at $\alpha_{J2000}=11^h20^m13.5^s$ and $\delta_{J2000}=13°00'17\rlap{.}''7$. Velocity-channels are displayed from v=−53.76 km s^{-1} to v=−148.26 km s^{-1} in steps of 3.26 km s^{-1}. Velocities are referred to the LSR scale and the zero velocity corresponds to v_0=712.6 km s^{-1}. Contour levels start from −20 mJy beam^{-1} with step of 20 mJy beam^{-1}. The rms noise is 3.4 mJy beam^{-1} and only regions whose brightness is larger than 6-σ are shown.
Lower panel: ^{12}CO(2-1) integrated intensity. Contours level start from 0.18 Jy km s^{-1} beam^{-1} and scale by a factor of $\sqrt{2}$.
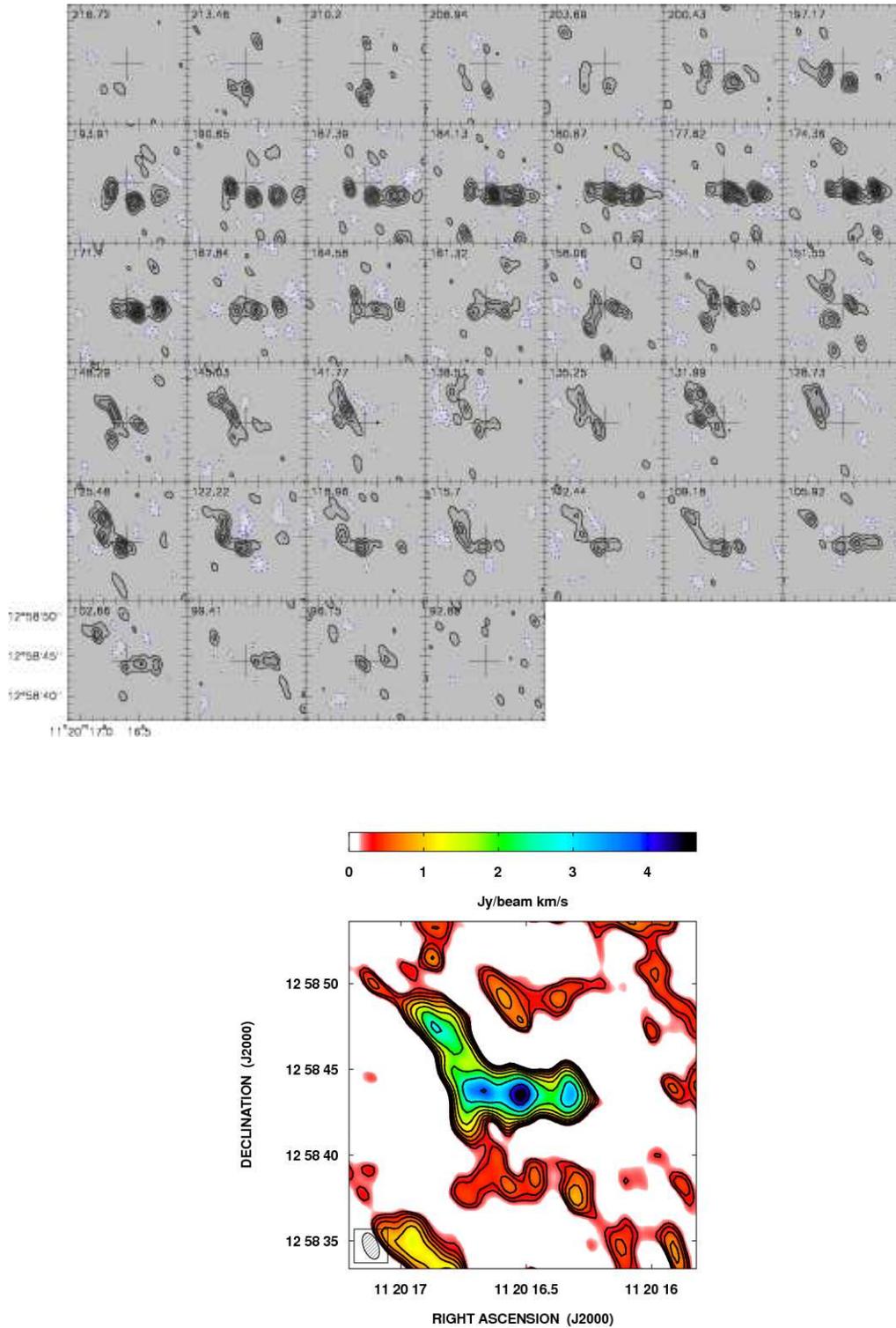
Fig. 16. South bar end of NGC 3627. *Upper panel*: ^{12}CO(2-1) velocity-channel maps observed with the PdBI. The spatial resolution is of $1''63 \times 0''87$ at PA=31°. We show a field of view of 15″. The phase tracking center is indicated by a cross at $\alpha_{J2000}=11^h20^m 16.6^s$ and $\delta_{J2000}=12°58'44''5$. Velocity-channels are displayed from v=216.72 km s^{-1} to v=92.89 km s^{-1} in steps of 3.26 km s^{-1}. Velocities are referred to the LSR and the zero velocity corresponds to v_0=712.6 km s^{-1}. Contour levels start from −20 mJy beam^{-1} with step of 20 mJy beam^{-1}. The rms noise is of 4 mJy beam^{-1} and only regions whose brightness is larger than 5-σ are shown.
Lower panel: South bar end of NGC 3627:^{12}CO(2-1) integrated intensity. Contours level start from 0.24 Jy km s^{-1} beam^{-1} and scale by a factor of $\sqrt{2}$.